

Research Article

Compression at the Source for Digital Camcorders

Nir Maor,¹ Arie Feuer,¹ and Graham C. Goodwin²

¹Department of Electrical Engineering (EE), Technion-Israel Institute of Technology, Haifa 32000, Israel

²School of Electrical Engineering and Computer Science, University of Newcastle, Callaghan NSW 2308, Australia

Received 2 October 2006; Accepted 30 March 2007

Recommended by Russell C. Hardie

Typical sensors (CCD or CMOS) used in home digital camcorders have the potential of generating high definition (HD) video sequences. However, the data read out rate is a bottleneck which, invariably, forces significant quality deterioration in recorded video clips. This paper describes a novel technology for achieving a better utilization of sensor capability, resulting in HD quality video clips with essentially the same hardware. The technology is based on the use of a particular type of nonuniform sampling strategy. This strategy combines infrequent high spatial resolution frames with more frequent low resolution frames. This combination allows the data rate constraint to be achieved while retaining an HD quality output. Post processing via filter banks is used to combine the high and low spatial resolution frames to produce the HD quality output. The paper provides full details of the reconstruction algorithm as well as proofs of all key supporting theories.

Copyright © 2007 Nir Maor et al. This is an open access article distributed under the Creative Commons Attribution License, which permits unrestricted use, distribution, and reproduction in any medium, provided the original work is properly cited.

1. INTRODUCTION: CURRENT TECHNOLOGY

In many digital systems, one faces the problem of having a source which generates data at a rate higher than that which can be transmitted over an associated communication channel. As a consequence, some means of compression are required at the source. A specific case of this problem arises in the current technology of digital home camcorders.

Figure 1 shows a schematic diagram of a typical digital camcorder. Images are captured on a two-dimensional sensor array (either CCD or CMOS). Each sensor in the array gives a spatial sample of the continuous image, a pixel, and the whole array gives a temporal sample of the time-varying image, a frame. The result is a 3D sampling process of a signal having two spatial dimensions and one temporal dimension. A hard constraint on the spatial resolution in each frame is determined by the number of sensors in the sensor array, while a hard constraint on the frame rate is determined by the minimum exposure time required by the sensor technology. The result is a uniformly sampled digital video sequence which perfectly captures a time-varying image whose spectrum is bandlimited to a box as shown in Figure 2. We note that the cross-sectional area of the box depends on the spatial resolution constraint, while the other dimension of the box depends on the maximal frame rate. As it turns out, the spectrum of typical time-varying images can reasonably be assumed to be contained in this box. Thus, the sensor

technology of most home digital camcorders can, in principle, generate video of high quality (high definition).

However, in current sensor technology, there is a third hard constraint, namely, the rate at which the data from the sensor can be read. This turns out to be the *dominant constraint* since this rate is typically lower than the rate of data generated by the sensor. Thus, downsampling (either spatially and/or temporally) is necessary to meet the read out constraint. In current technology, this downsampling is done *uniformly*. The result is a uniformly sampled digital video sequence (see Figure 1) which can perfectly capture only those scenes which have a spectrum limited to a box of considerably smaller dimensions. This is illustrated in Figure 3 where the box in dashed lines represents the full sensor capability and the solid box represents the reduced capability resulting from the use of uniform downsampling. The end result is quite often unsatisfactory due to the associated spatial and/or temporal information loss.

With the above as background, the question addressed in the current paper is whether a different compression mechanism can be utilized, which will lead to significantly less information loss. We show, in the sequel, that the technology we present achieves this goal. An important point is that the new mechanism does not require a new sensor array, but, instead, achieves a *better utilization of existing capabilities*. The idea thus yields resolution gains without requiring major hardware modification. (The core idea is the subject of

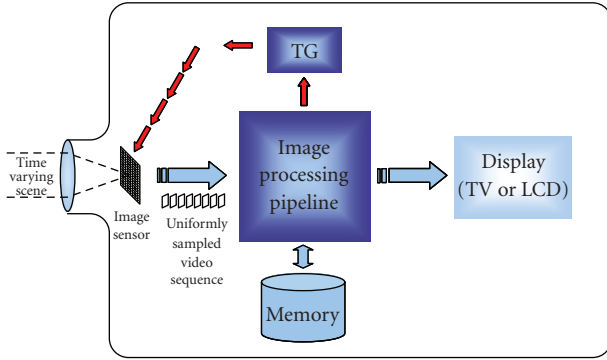


FIGURE 1: Schematics diagram of a typical digital camcorder.

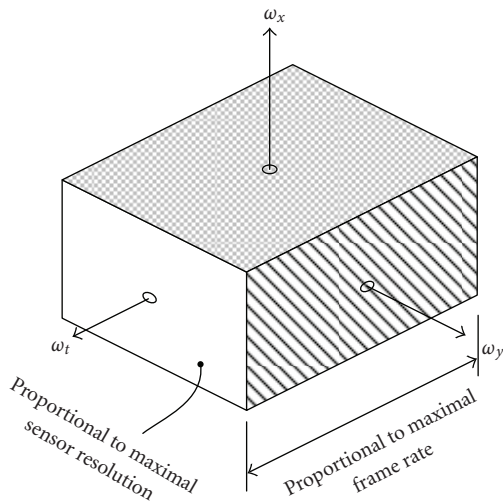


FIGURE 2: Sensor array potential capacity.

a recent patent application by a subset of the current authors [1].)

Previous relevant work includes the work done by Shechtman et al. [2]. In the latter paper, the authors use a number of camcorders recording the same scene, to overcome single camcorder limitations. Some of these camcorders have high spatial resolution but slow frame rate and others have reduced spatial resolution but high frame rate. The resulting data is fused to generate a single high quality video sequence (with high spatial resolution and fast frame rate). This approach has limited practical use because of the use of multiple camcorders. Also, the idea involves some technical difficulties such as the need to perform registration of the data from the different camcorders. The idea described in the current paper avoids these difficulties.

The layout of the remainder of the paper is as follows: in Section 2 we describe the spectral properties of typical video clips. This provides the basis for our approach as presented in Section 3. Note that we describe our approach both heuristically and formally. In Section 4 we present experimental

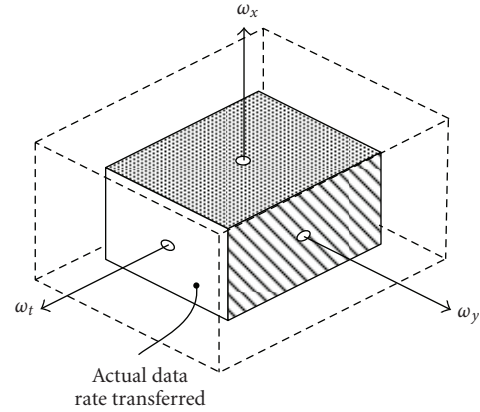
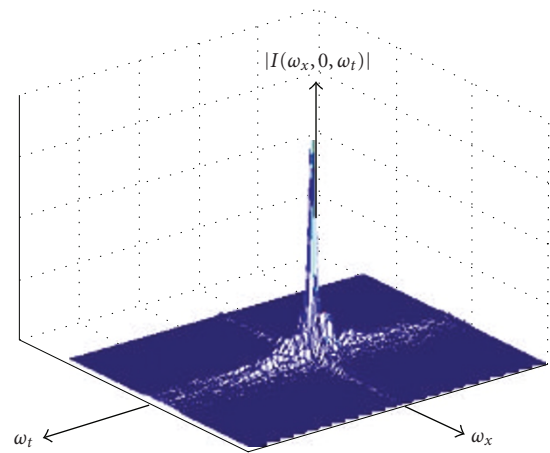


FIGURE 3: Digital camcorder actual capacity.

FIGURE 4: 3D spectrum of a typical video clip (shows only the ω_t and ω_x axes).

results using our approach. Finally, in Section 5 we provide conclusions.

2. VIDEO SPECTRAL PROPERTIES

The technology that we present here is based on the premise that the data read out rate, or equivalently, the volume in Figure 3, is a hard constraint. We deal with this constraint by modifying the downsampling scheme (data compression) so as to better fit the characteristics of the data. We do this by appropriate use of nonuniform sampling so as to avoid the redundancy inherent in uniform sampling. Background to this idea is contained in [3] which discusses the potential redundancy frequently associated with uniform sampling (see also [4]).

To support our idea we have conducted a thorough study of the spectral properties of over 150 typical video clips. To illustrate our findings, we show the spectrum of one of these clips in Figure 4. (We show only one of the spatial frequency axes with similar results for the second spatial frequency.) We note in this figure that the *spectral energy is concentrated*

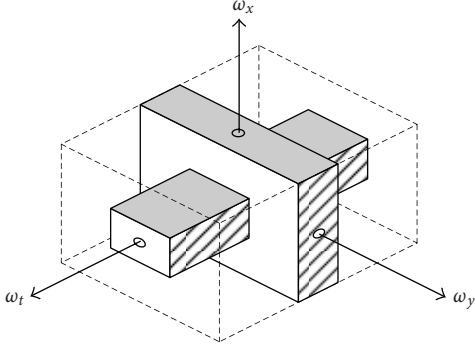


FIGURE 5: Spectral support shape of video clips.

around the spatial frequency plane and the temporal frequency axis. This characteristic is common to all clips studied. We will see in the sequel that this observation is, indeed, the cornerstone of our method.

To further support our key observation, we passed a large number of video clips through three ideal lowpass filters having spectral support of a fixed volume but different shapes. The first and second filters had a box-like support representing either uniform spatial or temporal decimation. A third filter had the more intricate shape shown in Figure 5. The outputs of these filters were compared both quantitatively (using PSNR) and qualitatively (by viewing the video clips) to the original input clip. On average, the third filter produced a 10 dB advantage over the other two. In all cases examined, the qualitative comparisons were even more favorable than suggested by the quantitative comparison. Full details of the study are presented in [5]. Our technology (as will be shown in the sequel) can accommodate more intricate shapes which may constitute a better fit to actual spectral supports. Indeed, we are currently experimenting with the dimensions and shape of the filter support as illustrated in Figure 5 to better fit the “foot print” of typical video spectra (see also Remark 2).

3. NONUNIFORMLY SAMPLED VIDEO

3.1. Heuristic explanation of the sampling strategy

By examining the spectral properties of typical video clips, as described in the previous section, we have observed that there is hardly any information which has simultaneously both high spatial and high temporal frequencies. This observation leads to the intuitive idea of interweaving a combination of two sequences: one of high spatial resolution but slow frame rate and a second with low spatial resolution but high frame rate. The result is a nonuniformly sampled video sequence as schematically depicted in Figure 6. Note that there is a time gap inserted following each of the high resolution frames since these frames require more time to be read out (see Remark 3). In the remainder of the paper, we will formally prove that sampling schemes of the type shown in Figure 6 do indeed allow perfect reconstruction of

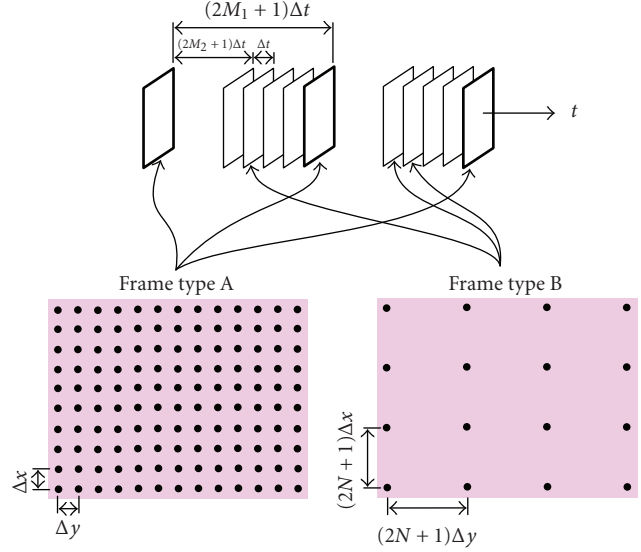


FIGURE 6: Nonuniformly sampled video sequence.

signals which have a frequency domain “footprint” of the type shown in Figure 5.

3.2. Perfect reconstruction from nonuniform sampled data

To develop the associated theoretical results, we will utilize ideas related to sampling lattices. For background on these concepts the reader is referred to [3, 6, 7]. A central tool in our discussion will be the multidimensional generalized sampling expansion (GSE). For completeness, we have included a brief (without proofs) exposition of the GSE in Appendix A. A more detailed discussion can be found in, for example, [3, 8, 9].

In the sequel, we will first demonstrate that the sampling pattern used (see Figure 6) is a form of recurrent sampling. We will then employ the GSE tool. In particular, we will utilize the idea that perfect reconstruction from a recurrent sampling is possible if the sampling pattern and the signal spectral support are such that the resulting matrix H (see (A. 24) in Appendix A) is nonsingular. Specifically, we will show that the sampling pattern in Figure 6 allows perfect reconstruction of signals having spectral support as in Figure 5.

To simplify the presentation we will consider only the case where one of the spatial dimensions is affected while the other spatial dimension is untouched during the process (namely, it has the full available spatial resolution of the sensor array). The extension to the more general case is straightforward but involves more complex notation. Thus, we will examine a sampling pattern of the type shown in Figure 7. Furthermore, to simplify notation, we let $\mathbf{z} = \begin{bmatrix} x \\ t \end{bmatrix}$. We also use Δx and Δt to represent full spatial and temporal resolution. However, we note that the use of these sampling intervals in a *uniform* pattern would lead to a data rate that could not be read off the sensor array.

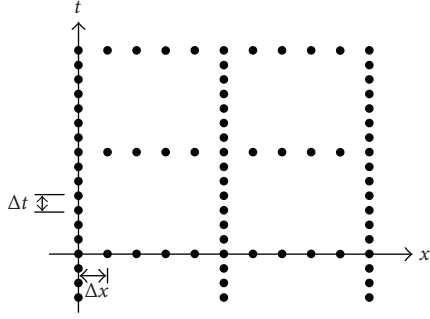


FIGURE 7: The nonuniform sampling pattern considered.

Also, to make the presentation easier, we will ignore the extra time interval after the high resolution frames as shown in Figure 5. (See also Remark 3.) More formally, we consider the sampling lattice

$$\mathcal{L}\mathcal{A}\mathcal{T}(T) = \{T\mathbf{n} : \mathbf{n} \in \mathbb{Z}^2\}, \quad (1)$$

where

$$T = \begin{bmatrix} (2L+1)\Delta x & 0 \\ 0 & (2M+1)\Delta t \end{bmatrix}. \quad (2)$$

In each unit cell of this lattice we add $2(L+M)$ samples

$$\left\{ \begin{bmatrix} \ell\Delta x \\ 0 \end{bmatrix} \right\}_{\ell=1}^{2L} \cup \left\{ \begin{bmatrix} 0 \\ m\Delta t \end{bmatrix} \right\}_{m=1}^{2M} \quad (3)$$

to obtain the sampling pattern

$$\Psi = \bigcup_{q=1}^{2(L+M)+1} \{\mathcal{L}\mathcal{A}\mathcal{T}(T) + \mathbf{z}_q\}, \quad (4)$$

where

$$\mathbf{z}_q = \begin{cases} \mathbf{0}, & \text{for } q = 1, \\ \begin{bmatrix} (q-1)\Delta x \\ 0 \end{bmatrix}, & \text{for } q = 2, \dots, 2L+1, \\ \begin{bmatrix} 0 \\ (q-2L-1)\Delta t \end{bmatrix}, & \text{for } q = 2(L+1), \dots, \\ & 2(L+M)+1. \end{cases} \quad (5)$$

As shown in Appendix A this constitutes a recurrent sampling pattern. Moreover, we readily observe that this is exactly the sampling pattern portrayed in Figure 7 (for $L = 2$ and $M = 3$). (Note that, for these values, every seventh frame has full resolution while, in the low resolution frames, only every fifth line is read.) The unit cell we consider for the reciprocal lattice, $\mathcal{L}\mathcal{A}\mathcal{T}(2\pi T^{-T}) = \{2\pi T^{-T}\mathbf{n} : \mathbf{n} \in \mathbb{Z}^2\}$, is

$$\begin{aligned} & \mathcal{UC}(2\pi T^{-T}) \\ &= \left\{ \boldsymbol{\omega} : |\omega_x| < \frac{\pi}{(2L+1)\Delta x}, |\omega_t| < \frac{\pi}{(2M+1)\Delta t} \right\}. \end{aligned} \quad (6)$$

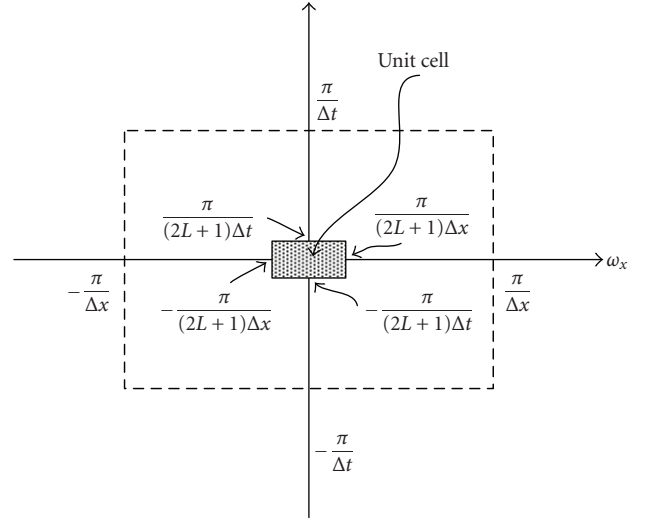


FIGURE 8: Unit cell of reciprocal lattice.

This is illustrated in Figure 8. (Note that the dashed box in the figure represents the sensor data generation capacity which, as previously noted, exceeds the data transition capability.) We next construct the set

$$\mathcal{S} = \bigcup_{p=1}^{2(L+M)+1} \{\mathcal{UC}(2\pi T^{-T}) + \mathbf{c}_p\}, \quad (7)$$

where

$$\mathbf{c}_p = \begin{cases} \mathbf{0}, & \text{for } p = 1, \\ \begin{bmatrix} \frac{2\pi(p-1)}{(2L+1)\Delta x} \\ 0 \end{bmatrix}, & \text{for } p = 2, \dots, L+1, \\ \begin{bmatrix} \frac{2\pi(L+1-p)}{(2L+1)\Delta x} \\ 0 \end{bmatrix}, & \text{for } p = L+2, \dots, 2L+1, \\ \begin{bmatrix} 0 \\ \frac{2\pi(p-2L-1)}{(2M+1)\Delta t} \end{bmatrix}, & \text{for } p = 2L+2, \dots, \\ & 2L+M+1, \\ \begin{bmatrix} 0 \\ \frac{2\pi(2L+M+1-p)}{(2M+1)\Delta t} \end{bmatrix}, & \text{for } p = 2L+M+2, \dots, \\ & 2(L+M)+1. \end{cases} \quad (8)$$

This set is illustrated in Figure 9. We observe that the set in Figure 9 is, in fact, a cross-section of the set in Figure 5 (at $\omega_y = 0$). We are now ready to state our main technical result.

Theorem 1. Let $I(\mathbf{z})$ be a signal bandlimited to the set \mathcal{S} as given in (7) and let this signal be sampled on Ψ as given in (4).

Then, $I(\mathbf{z})$ can be perfectly reconstructed from the sampled data $\{I(\tilde{\mathbf{z}})\}_{\tilde{\mathbf{z}} \in \Psi}$.

Proof. See Appendix B. \square

Theorem 1 establishes our key claim, namely, that perfect reconstruction is indeed possible using the proposed nonuniform sampling pattern. We next give an explicit form for the reconstruction.

Theorem 2. *With assumptions as in Theorem 1, perfect signal reconstruction can be achieved using*

$$I(\mathbf{z}) = \sum_{\mathbf{n} \in \mathbb{Z}^2} \sum_{q=1}^{2(L+M)+1} I(T\mathbf{n} + \mathbf{z}_q) \varphi_q(\mathbf{z} - T\mathbf{n}), \quad (9)$$

where $\varphi_q(\mathbf{z})$ has the form

$$\varphi_1(\mathbf{z}) = \left[\begin{aligned} & \left(\frac{1}{2L+1} + \frac{1}{2M+1} - 1 \right) \\ & + \frac{1}{2L+1} \frac{2 \sin\left(\frac{\pi Lx}{(2L+1)\Delta x}\right) \cos\left(\frac{\pi(L+1)x}{(2L+1)\Delta x}\right)}{\sin\left(\frac{\pi x}{(2L+1)\Delta x}\right)} \\ & + \frac{1}{2M+1} \frac{2 \sin\left(\frac{\pi Mt}{(2M+1)\Delta t}\right) \cos\left(\frac{\pi(M+1)t}{(2M+1)\Delta t}\right)}{\sin\left(\frac{\pi t}{(2M+1)\Delta t}\right)} \end{aligned} \right] \\ \times \frac{\sin\left(\frac{\pi x}{(2L+1)\Delta x}\right) \sin\left(\frac{\pi t}{(2M+1)\Delta t}\right)}{\frac{\pi x}{(2L+1)\Delta x} \frac{\pi t}{(2M+1)\Delta t}}, \\ \varphi_q(\mathbf{z}) = \begin{cases} \frac{\sin\left(\frac{\pi}{\Delta x}(x - (q-1)\Delta x)\right) \sin\left(\frac{\pi t}{(2M+1)\Delta t}\right)}{\frac{\pi}{\Delta x}(x - (q-1)\Delta x) \frac{\pi t}{(2M+1)\Delta t}}, & \text{for } q = 2, \dots, 2L+1, \\ \frac{\sin\left(\frac{\pi x}{(2L+1)\Delta x}\right) \sin\left(\frac{\pi}{\Delta t}(t - (q-2L-1)\Delta t)\right)}{\frac{\pi x}{(2L+1)\Delta x} \frac{\pi}{\Delta t}(t - (q-2L-1)\Delta t)}, & \text{for } q = 2(L+1), \dots, 2(L+M)+1. \end{cases} \quad (10)$$

Proof. See Appendix C. \square

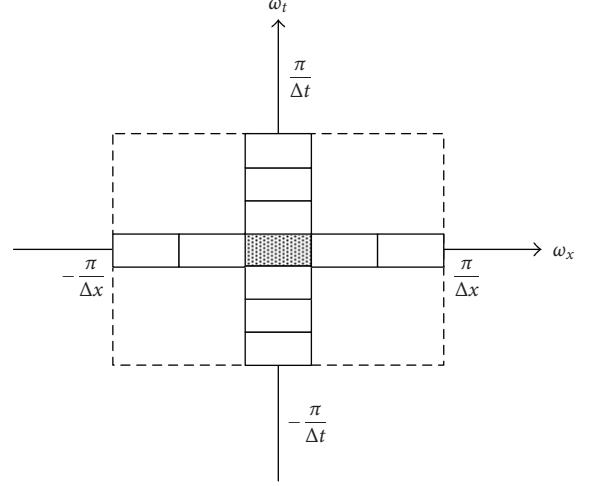


FIGURE 9: The spectrum covering set \mathcal{S} .

The reconstruction formula (9) can be rewritten as

$$\begin{aligned} I(\mathbf{z}) &= \sum_{\mathbf{n} \in \mathbb{Z}^2} \sum_{q=1}^{2(L+M)+1} I_q(T\mathbf{n}) \varphi_q(\mathbf{z} - T\mathbf{n}) \\ &= \sum_{q=1}^{2(L+M)+1} \left[I_q(\mathbf{z}) \sum_{\mathbf{n} \in \mathbb{Z}^2} \delta(\mathbf{z} - T\mathbf{n}) \right] * \varphi_q(\mathbf{z}) \\ &= \sum_{q=1}^{2(L+M)+1} I_q^d(\mathbf{z}) * \varphi_q(\mathbf{z}), \end{aligned} \quad (11)$$

where $I_q(\mathbf{z}) = I(\mathbf{z} + \mathbf{z}_q)$ is the original continuous signal shifted by \mathbf{z}_q and $I_q^d(\mathbf{z}) = I_q(\mathbf{z}) \sum_{\mathbf{n} \in \mathbb{Z}^2} \delta(\mathbf{z} - T\mathbf{n})$ is its (impulse) sampled version (on the lattice $\mathcal{L}\mathcal{A}\mathcal{T}(T)$). We see that the reconstruction can be viewed as having $2(L+M)+1$ signals, each passing through a filter with impulse response $\varphi_q(\mathbf{z})$. The outputs of these filters are then summed to produce the final result. A further embellishment is possible on noting that, in practice, we are usually not interested in achieving a continuous final result of the type described above. Rather, we wish to generate a high resolution, uniformly sampled video clip which can be fed into a digital high resolution display device. Specifically, say that we are interested in obtaining samples on the lattice $\{I(T_1)\}_{\mathbf{m} \in \mathbb{Z}^2}$, where

$$T_1 = \begin{bmatrix} \Delta x & 0 \\ 0 & \Delta t \end{bmatrix}. \quad (12)$$

Note that $\mathcal{L}\mathcal{A}\mathcal{T}(T)$ is a strict subset of $\mathcal{L}\mathcal{A}\mathcal{T}(T_1)$. Thus, our goal is to convert the nonuniformly sampled data to a (high resolution) uniformly sampled data. This can be directly achieved by utilizing (11). Specifically, from (11), we obtain

$$I(T_1\mathbf{m}) = \sum_{q=1}^{2(L+M)+1} \sum_{\mathbf{k} \in \mathbb{Z}^2} \tilde{I}_q(T_1\mathbf{k}) \varphi_q(T_1(\mathbf{m} - \mathbf{k})) \quad (13)$$

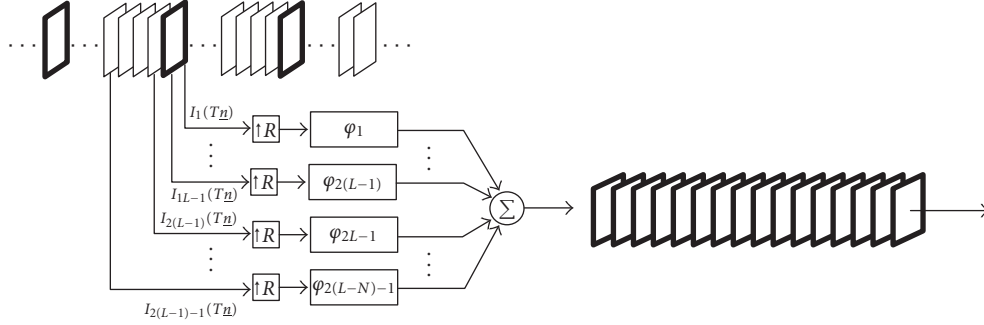


FIGURE 10: The reconstruction process.

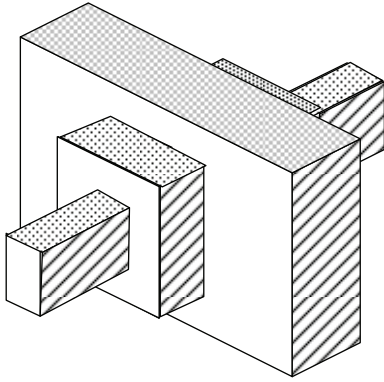


FIGURE 11: Alternative spectral covering set.

which is the discrete equivalent of (11). $\tilde{I}_q(T_1 \mathbf{k})$ denotes the zero-padded (interpolated) version of $I_q(T \mathbf{n})$. (This is easily seen since $\mathcal{L}\mathcal{A}\mathcal{T}(T) \subset \mathcal{L}\mathcal{A}\mathcal{T}(T_1)$.) This process is illustrated in Figure 10.

Remark 1. The compression achieved by the use of the specific sampling patterns and spectral covering sets described above is given by

$$\alpha = \frac{2(L+M)+1}{(2L+1)(2M+1)}. \quad (14)$$

Remark 2. Heuristically, we could achieve even greater compression by using more detailed information about typical video spectral “footprints.” Ongoing work is aimed at finding nonuniform sampling patterns which apply to more general spectral covering sets. Figure 11 illustrates a possible spectral “footprint.”

Remark 3. As noted earlier, we have assumed in the above development that a fixed time interval is used between all frames. This was done for the ease of exposition. A parallel derivation for the case when these intervals are not equal (as in Figure 6) has been carried out and is presented in [5]. Indeed, this more general scheme was used in all our experiments.



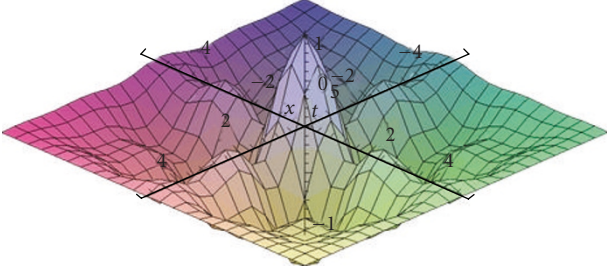
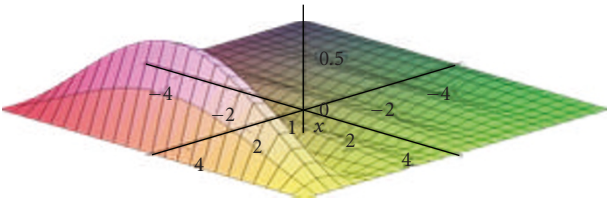
FIGURE 12: Frames from original clip.

4. EXAMPLE

To illustrate the potential benefits of our approach we chose a clip consisting of 320 by 240 pixels per frame at 30 frames per second—Figure 12 shows six frames out of this clip. The pixel rate of this clip is 2304000 pixels per second. We create a nonuniformly sampled sequence by using the methods described in Section 3 with $L = M = 2$. The resulting compression ratio is (see (14)) 9/25. The reconstruction functions in this case are

$$\begin{aligned} \varphi_1(\mathbf{z}) &= 5 \left[-3 + \frac{2 \sin \frac{2\pi x}{5\Delta x} \cos \frac{3\pi x}{5\Delta x}}{\sin \frac{\pi x}{5\Delta x}} + \frac{2 \sin \frac{2\pi t}{5\Delta t} \cos \frac{3\pi t}{5\Delta t}}{\sin \frac{\pi t}{5\Delta t}} \right] \\ &\quad \times \frac{\sin \frac{\pi x}{5\Delta x}}{\Delta x} \frac{\sin \frac{\pi t}{5\Delta t}}{\Delta t}, \\ \varphi_q(\mathbf{z}) &= \frac{\sin \frac{\pi(x - (q-1)\Delta x)}{\Delta x}}{\pi(x - (q-1)\Delta x)} \frac{\sin \frac{\pi t}{5\Delta t}}{\pi t / 5\Delta t}, \quad \text{for } q = 2, 3, 4, 5, \\ \varphi_q(\mathbf{z}) &= \frac{\sin \frac{\pi x}{5\Delta x}}{\pi x} \frac{\sin \frac{\pi(t - (q-5)\Delta t)}{\Delta t}}{\pi(t - (q-5)\Delta t) / \Delta t}, \quad \text{for } q = 6, 7, 8, 9. \end{aligned} \quad (15)$$

Figures 13 and 14 show $\varphi_1(\mathbf{z})$ and $\varphi_5(\mathbf{z})$. Using these functions we have reconstructed the clip. Figure 15 shows the reconstructed frames corresponding to the frames in Figure 12. We observe that the reconstructed frames are almost identical (both spatially and temporally) to the frames from the original clip.

FIGURE 13: $\varphi_1(\mathbf{z})$.FIGURE 14: $\varphi_5(\mathbf{z})$.

To illustrate that our method offers advantages relative to other strategies, we also tested *uniform spatial decimation* achieved by removing, in all frames, 3 out of every 5 columns. This results in a compression ratio of ~ 0.4 ($> 9/25$). While the compression ratio is larger (less compression), the resulting clip is of significantly poorer quality as can be seen in the frames of Figure 16. We also applied temporal decimation by removing 3 out of every 5 frames resulting again in a compression ratio of 0.4. Temporal interpolation was then used to fill up the missing frames. The results are shown in Figure 17. We note that the reconstructed motion differs from the original one (see fourth and sixth frames from the left).

5. CONCLUSIONS

This paper has addressed the problem of under utilization of sensor capabilities in digital camcorders arising from constrained data read out rate. Accepting the data read out rate as a hard constraint of a camcorder, it has been shown that, by generating a nonuniformly sampled digital video sequence, it is possible to generate improved resolution video clips with the same read out rate. The approach presented here utilizes prior information regarding the “footprint” of typical video clip spectra. Specifically, we have exploited the observation that high spatial frequencies seldom occur simultaneously with high temporal frequencies. Reconstruction of an improved resolution (both spatial and temporal) digital video clip from the nonuniform samples has been presented in a form of a filter bank.



FIGURE 15: Frames from reconstructed clip.



FIGURE 16: Frames from the spatially decimated clip.



FIGURE 17: Frames from the temporally decimated clip.

APPENDICES

A. MULTIDIMENSIONAL GSE

A.1. General

Consider a bandlimited signal $f(\mathbf{z})$, $\mathbf{z} \in \mathbb{R}^D$, and a sampling lattice $\mathcal{L}\mathcal{A}\mathcal{T}(T)$. Assume that $\mathcal{L}\mathcal{A}\mathcal{T}(T)$ is not a Nyquist lattice for $f(\mathbf{z})$, namely, the signal *cannot be reconstructed* from its samples on this lattice. Let $\mathcal{UC}(2\pi T^{-T})$ be a unit cell for the reciprocal lattice $\mathcal{L}\mathcal{A}\mathcal{T}(2\pi T^{-T})$. Then, there always exists a set of points $\{\mathbf{c}_p\}_{p=1}^P \subset \mathcal{L}\mathcal{A}\mathcal{T}(2\pi T^{-T})$ such that

$$\text{support } \{\hat{f}(\boldsymbol{\omega})\} \subset \bigcup_{p=1}^P \{\mathcal{UC}(2\pi T^{-T}) + \mathbf{c}_p\}. \quad (\text{A. 16})$$

Suppose now that the signal is passed through a bank of shift-invariant filters $\{\hat{h}_q(\boldsymbol{\omega})\}_{q=1}^Q$ and the filter outputs $f_q(\mathbf{z})$ are then sampled on the given lattice to generate the data set $\{f_q(T\mathbf{n})\}_{\mathbf{n} \in \mathbb{Z}^D, q=1, \dots, Q}$. We then have the following result.

Theorem 3. *The signal $f(\mathbf{z})$, under assumption (A. 16), can be reconstructed from the data set $\{f_q(T\mathbf{n})\}_{\mathbf{n} \in \mathbb{Z}^D, q=1, \dots, Q}$ if and only if the matrix*

$$\mathcal{H}(\boldsymbol{\omega}) = \begin{bmatrix} \hat{h}_1(\boldsymbol{\omega} + \mathbf{c}_1) & \hat{h}_2(\boldsymbol{\omega} + \mathbf{c}_1) & \cdots & \hat{h}_Q(\boldsymbol{\omega} + \mathbf{c}_1) \\ \hat{h}_1(\boldsymbol{\omega} + \mathbf{c}_2) & \hat{h}_2(\boldsymbol{\omega} + \mathbf{c}_2) & \cdots & \hat{h}_Q(\boldsymbol{\omega} + \mathbf{c}_2) \\ \vdots & \vdots & \ddots & \vdots \\ \hat{h}_1(\boldsymbol{\omega} + \mathbf{c}_P) & \hat{h}_2(\boldsymbol{\omega} + \mathbf{c}_P) & \cdots & \hat{h}_Q(\boldsymbol{\omega} + \mathbf{c}_P) \end{bmatrix} \in \mathbb{C}^{P \times Q} \quad (\text{A. 17})$$

has full row rank for all $\boldsymbol{\omega} \in \mathcal{UC}(2\pi T^{-T})$. The reconstruction formula is given by

$$f(\mathbf{z}) = \sum_{q=1}^Q \sum_{\mathbf{n} \in \mathbb{Z}^D} f_q(T\mathbf{n}) \varphi_q(\mathbf{z} - T\mathbf{n}), \quad (\text{A. 18})$$

where

$$\varphi_q(\mathbf{z}) = \frac{|\det T|}{(2\pi)^D} \int_{\mathcal{UC}(2\pi T^{-T})} \Phi_q(\boldsymbol{\omega}, \mathbf{z}) e^{j\boldsymbol{\omega}^T \mathbf{z}} d\boldsymbol{\omega} \quad (\text{A. 19})$$

and where $\Phi_q(\boldsymbol{\omega}, \mathbf{z})$ are the solutions of the following set of linear equations:

$$\mathcal{H}(\boldsymbol{\omega}) \begin{bmatrix} \Phi_1(\boldsymbol{\omega}, \mathbf{z}) \\ \Phi_2(\boldsymbol{\omega}, \mathbf{z}) \\ \vdots \\ \Phi_Q(\boldsymbol{\omega}, \mathbf{z}) \end{bmatrix} = \begin{bmatrix} e^{j\mathbf{c}_1^T \mathbf{z}} \\ e^{j\mathbf{c}_2^T \mathbf{z}} \\ \vdots \\ e^{j\mathbf{c}_P^T \mathbf{z}} \end{bmatrix}. \quad (\text{A. 20})$$

A.2. Perfect reconstruction from recurrent sampling

The above GSE result can be applied to reconstruction from recurrent sampling. By recurrent sampling we refer to a sampling pattern Ψ given by

$$\Psi = \bigcup_{q=1}^Q \{\mathcal{L}\mathcal{A}\mathcal{T}(T) + \mathbf{z}_q\}, \quad (\text{A. 21})$$

where, w.l.o.g. we assume that $\{\mathbf{z}_q\} \subset \mathcal{UC}(T)$. (Otherwise, one can redefine them as $\mathbf{z}_q - T\mathbf{n}_q \in \mathcal{UC}(T)$ and Ψ will remain the same.) The data set we have is $\{f(\tilde{\mathbf{z}})\}_{\tilde{\mathbf{z}} \in \Psi}$ and our goal is to perfectly reconstruct $f(\mathbf{z})$.

Let us define $\hat{h}_q(\boldsymbol{\omega}) = e^{j\boldsymbol{\omega}^T \mathbf{z}_q}$, then $f_q(\mathbf{z}) = f(\mathbf{z} + \mathbf{z}_q)$ and

$$\{f_q(T\mathbf{n})\}_{\mathbf{n} \in \mathbb{Z}^D, q=1, \dots, Q} = \{f(\tilde{\mathbf{z}})\}_{\tilde{\mathbf{z}} \in \Psi}. \quad (\text{A. 22})$$

Thus, we can apply the GSE reconstruction. In the current case

$$\begin{aligned} \mathcal{H}(\boldsymbol{\omega}) &= \begin{bmatrix} e^{j(\boldsymbol{\omega} + \mathbf{c}_1)^T \mathbf{z}_1} & e^{j(\boldsymbol{\omega} + \mathbf{c}_1)^T \mathbf{z}_2} & \dots & e^{j(\boldsymbol{\omega} + \mathbf{c}_1)^T \mathbf{z}_Q} \\ e^{j(\boldsymbol{\omega} + \mathbf{c}_2)^T \mathbf{z}_1} & e^{j(\boldsymbol{\omega} + \mathbf{c}_2)^T \mathbf{z}_2} & \dots & e^{j(\boldsymbol{\omega} + \mathbf{c}_2)^T \mathbf{z}_Q} \\ \vdots & \vdots & \ddots & \vdots \\ e^{j(\boldsymbol{\omega} + \mathbf{c}_P)^T \mathbf{z}_1} & e^{j(\boldsymbol{\omega} + \mathbf{c}_P)^T \mathbf{z}_2} & \dots & e^{j(\boldsymbol{\omega} + \mathbf{c}_P)^T \mathbf{z}_Q} \end{bmatrix} \\ &= H \cdot \text{diag}\{e^{j\boldsymbol{\omega}^T \mathbf{z}_1}, \dots, e^{j\boldsymbol{\omega}^T \mathbf{z}_Q}\}, \end{aligned} \quad (\text{A. 23})$$

where

$$H = \begin{bmatrix} e^{j\mathbf{c}_1^T \mathbf{z}_1} & e^{j\mathbf{c}_1^T \mathbf{z}_2} & \dots & e^{j\mathbf{c}_1^T \mathbf{z}_Q} \\ e^{j\mathbf{c}_2^T \mathbf{z}_1} & e^{j\mathbf{c}_2^T \mathbf{z}_2} & \dots & e^{j\mathbf{c}_2^T \mathbf{z}_Q} \\ \vdots & \vdots & \ddots & \vdots \\ e^{j\mathbf{c}_P^T \mathbf{z}_1} & e^{j\mathbf{c}_P^T \mathbf{z}_2} & \dots & e^{j\mathbf{c}_P^T \mathbf{z}_Q} \end{bmatrix} \in \mathbb{C}^{P \times Q}. \quad (\text{A. 24})$$

Note that the matrix $\text{diag}\{e^{j\boldsymbol{\omega}^T \mathbf{z}_1}, \dots, e^{j\boldsymbol{\omega}^T \mathbf{z}_Q}\}$ is always nonsingular, hence, by Theorem 3, perfect reconstruction is possible if and only if H has full row rank. Clearly, a necessary condition is $Q \geq P$. For simplicity, one often uses $Q = P$.

B. PROOF OF THEOREM 1

The sampling pattern described in (4) is clearly a recurrent sampling pattern. We can thus apply the result of Theorem 3. As the discussion in Appendix A.2 concludes, all we need to

show is that the matrix H in (A. 24) is nonsingular. We note that here we have $Q = P = 2(L + M) + 1$. By the definitions of $\{\mathbf{z}_q\}_{q=1}^{2(L+M)+1}$ and $\{\mathbf{c}_p\}_{p=1}^{2(L+M)+1}$ in (4) and (8), respectively, we observe that the resulting matrix H can be written as

$$H = \begin{bmatrix} \mathbf{1} & \mathbf{1}_{2(L+M)}^T \\ \mathbf{1}_{2(L+M)} & \tilde{H} \end{bmatrix}, \quad (\text{A. 25})$$

where $\mathbf{1}_P$ denotes a P -dimensional vector of ones and

$$\tilde{H} = \begin{bmatrix} A & \mathbf{1}_{2L} \mathbf{1}_{2M}^T \\ \mathbf{1}_{2M} \mathbf{1}_{2L}^T & B \end{bmatrix}, \quad (\text{A. 26})$$

$$A_{p,q} = \begin{cases} e^{j(2\pi/(2L+1))qp}, & \\ \text{for } p = 1, 2, \dots, L, & q = 1, 2, \dots, 2L \\ e^{j(2\pi/(2L+1))q(L-p)}, & \\ \text{for } p = L + 1, 2, \dots, 2L, & \end{cases} \quad (\text{A. 27})$$

$$B_{p,q} = \begin{cases} e^{j(2\pi/(2M+1))qp}, & \\ \text{for } p = 1, 2, \dots, M, & q = 1, 2, \dots, 2M \\ e^{j(2\pi/(2M+1))q(M-p)}, & \\ \text{for } p = M + 1, 2, \dots, 2M, & \end{cases} \quad (\text{A. 28})$$

From (A. 25) we can readily show that

$$\begin{aligned} H^{-1} &= [1 + \mathbf{1}_{2(L+M)}^T (\tilde{H} - \mathbf{1}_{2(L+M)} \mathbf{1}_{2(L+M)}^T)^{-1} \mathbf{1}_{2(L+M)} \\ &\quad - (\tilde{H} - \mathbf{1}_{2(L+M)} \mathbf{1}_{2(L+M)}^T)^{-1} \mathbf{1}_{2(L+M)} \\ &\quad - \mathbf{1}_{2(L+M)}^T (\tilde{H} - \mathbf{1}_{2(L+M)} \mathbf{1}_{2(L+M)}^T)^{-1} \\ &\quad \times (\tilde{H} - \mathbf{1}_{2(L+M)} \mathbf{1}_{2(L+M)}^T)^{-1}]. \end{aligned} \quad (\text{A. 29})$$

Hence, H^{-1} exists if and only if $(\tilde{H} - \mathbf{1}_{2(L+M)} \mathbf{1}_{2(L+M)}^T)^{-1}$ exists. Using (A. 26) we can write (A. 27) and (A. 28) as

$$\begin{aligned} &(\tilde{H} - \mathbf{1}_{2(L+M)} \mathbf{1}_{2(L+M)}^T)^{-1} \\ &= \begin{bmatrix} (A - \mathbf{1}_{2L} \mathbf{1}_{2L}^T)^{-1} & 0 \\ 0 & (B - \mathbf{1}_{2M} \mathbf{1}_{2M}^T)^{-1} \end{bmatrix}. \end{aligned} \quad (\text{A. 30})$$

Hence, we need to establish that $(A - \mathbf{1}_{2L} \mathbf{1}_{2L}^T)^{-1}$ and $(B - \mathbf{1}_{2M} \mathbf{1}_{2M}^T)^{-1}$ exist. Using the definitions of A and B in (A. 27) and (A. 28) we can readily show that

$$A^H A = A A^H = (2L + 1)I_{2L} - \mathbf{1}_{2L} \mathbf{1}_{2L}^T, \quad (\text{A. 31})$$

$$B^H B = B B^H = (2m + 1)I_{2M} - \mathbf{1}_{2M} \mathbf{1}_{2M}^T,$$

$$A \mathbf{1}_{2L} = A^H \mathbf{1}_{2L} = -\mathbf{1}_{2L}, \quad (\text{A. 32})$$

$$B \mathbf{1}_{2M} = B^H \mathbf{1}_{2M} = -\mathbf{1}_{2M},$$

where $(\cdot)^H$ denotes the transpose conjugate of (\cdot) . Hence,

$$A^{-1} = \frac{1}{2L+1} (A - \mathbf{1}_{2L} \mathbf{1}_{2L}^T), \quad (\text{A. 33})$$

$$B^{-1} = \frac{1}{2M+1} (B - \mathbf{1}_{2M} \mathbf{1}_{2M}^T)$$

so that

$$(A - \mathbf{1}_{2L} \mathbf{1}_{2L}^T)^{-1} = \frac{1}{2L+1} A^H, \quad (\text{A. 34})$$

$$(B - \mathbf{1}_{2M} \mathbf{1}_{2M}^T)^{-1} = \frac{1}{2M+1} B^H.$$

This establishes that these inverses exist. Hence, the inverse of H also exists. This completes the proof.

C. PROOF OF THEOREM 2

The proof follows from a straightforward application of the GSE results of Theorem 3 to the case at hand.

We first combine (A. 29), (A. 30), (A. 32), and (A. 34) to obtain

$$H^{-1} = \begin{bmatrix} 1 - \frac{2L}{2L+1} - \frac{2M}{2M+1} & \frac{1}{2L+1} \mathbf{1}_{2L}^T & \frac{1}{2M+1} \mathbf{1}_{2M}^T \\ \frac{1}{2L+1} \mathbf{1}_{2L} & \frac{1}{2L+1} A^H & 0 \\ \frac{1}{2M+1} \mathbf{1}_{2M} & 0 & \frac{1}{2M+1} B^H \end{bmatrix}. \quad (\text{A. 35})$$

Denoting

$$\boldsymbol{\gamma}_1(\mathbf{z}) = \begin{bmatrix} e^{j\mathbf{c}_2^T \mathbf{z}} \\ e^{j\mathbf{c}_3^T \mathbf{z}} \\ \vdots \\ e^{j\mathbf{c}_{2L+1}^T \mathbf{z}} \end{bmatrix}, \quad \boldsymbol{\gamma}_2(\mathbf{z}) = \begin{bmatrix} e^{j\mathbf{c}_{2(L+1)}^T \mathbf{z}} \\ e^{j\mathbf{c}_3^T \mathbf{z}} \\ \vdots \\ e^{j\mathbf{c}_{2(L+M)+1}^T \mathbf{z}} \end{bmatrix} \quad (\text{A. 36})$$

we can use (A. 20) and (A. 23) to obtain

$$\begin{bmatrix} \Phi_1(\boldsymbol{\omega}, \mathbf{z}) \\ \Phi_2(\boldsymbol{\omega}, \mathbf{z}) \\ \vdots \\ \Phi_{2(L+M)+1}(\boldsymbol{\omega}, \mathbf{z}) \end{bmatrix} = \text{diag} \{ e^{-j\boldsymbol{\omega}^T \mathbf{z}_1}, \dots, e^{-j\boldsymbol{\omega}^T \mathbf{z}_{2(L+M)+1}} \} \cdot H^{-1} \begin{bmatrix} 1 \\ \boldsymbol{\gamma}_1(\mathbf{z}) \\ \boldsymbol{\gamma}_2(\mathbf{z}) \end{bmatrix} \quad (\text{A. 37})$$

so that by (A. 35),

$$\begin{bmatrix} \Phi_1(\boldsymbol{\omega}, \mathbf{z}) \\ \Phi_2(\boldsymbol{\omega}, \mathbf{z}) \\ \vdots \\ \Phi_{2(L+M)+1}(\boldsymbol{\omega}, \mathbf{z}) \end{bmatrix} = \begin{bmatrix} e^{-j\boldsymbol{\omega}^T \mathbf{z}_1} \left(1 - \frac{2L}{2L+1} - \frac{2M}{2M+1} + \frac{1}{2L+1} \mathbf{1}_{2L}^T \boldsymbol{\gamma}_1(\mathbf{z}) + \frac{1}{2M+1} \mathbf{1}_{2M}^T \boldsymbol{\gamma}_2(\mathbf{z}) \right) \\ \text{diag} \{ e^{-j\boldsymbol{\omega}^T \mathbf{z}_2}, \dots, e^{-j\boldsymbol{\omega}^T \mathbf{z}_{2L+1}} \} \left(\frac{1}{2L+1} \mathbf{1}_{2L} + \frac{1}{2L+1} A^H \boldsymbol{\gamma}_1(\mathbf{z}) \right) \\ \text{diag} \{ e^{-j\boldsymbol{\omega}^T \mathbf{z}_{2(L+1)}}, \dots, e^{-j\boldsymbol{\omega}^T \mathbf{z}_{2(L+M)+1}} \} \left(\frac{1}{2M+1} \mathbf{1}_{2M} + \frac{1}{2M+1} B^H \boldsymbol{\gamma}_2(\mathbf{z}) \right) \end{bmatrix}. \quad (\text{A. 38})$$

From (8) and (A. 36) we have

$$\begin{aligned} \mathbf{1}_{2L}^T \boldsymbol{\gamma}_1(\mathbf{z}) &= \sum_{p=2}^{2L+1} e^{j\mathbf{c}_p^T \mathbf{z}} \\ &= \sum_{r=1}^L (e^{j(2\pi r x / ((2L+1)\Delta x))} + e^{-j(2\pi r x / ((2L+1)\Delta x))}) \\ &= \frac{2 \sin\left(\frac{\pi L x}{(2L+1)\Delta x}\right) \cos\left(\frac{\pi(L+1)x}{(2L+1)\Delta x}\right)}{\sin\left(\frac{\pi x}{(2L+1)\Delta x}\right)} \end{aligned} \quad (\text{A. 39})$$

and similarly

$$\mathbf{1}_{2M}^T \boldsymbol{\gamma}_2(\mathbf{z}) = \frac{2 \sin\left(\frac{\pi M t}{(2M+1)\Delta t}\right) \cos\left(\frac{\pi(M+1)t}{(2M+1)\Delta t}\right)}{\sin\left(\frac{\pi t}{(2M+1)\Delta t}\right)}. \quad (\text{A. 40})$$

Also, from (8), (A. 27), and (A. 36) we obtain, after some algebra,

$$\begin{aligned} (A^H \boldsymbol{\gamma}_1(\mathbf{z}))_r &= \sum_{s=1}^L (e^{-j(2\pi r s / (2L+1))} e^{j(2\pi s x / ((2L+1)\Delta x))} \\ &\quad + e^{j(2\pi r s / (2L+1))} e^{-j(2\pi s x / ((2L+1)\Delta x))}) \\ &= \frac{2 \sin\left(\frac{\pi L(x - r\Delta x)}{(2L+1)\Delta x}\right) \cos\left(\frac{\pi(L+1)(x - r\Delta x)}{(2L+1)\Delta x}\right)}{\sin\left(\frac{\pi(x - r\Delta x)}{(2L+1)\Delta x}\right)} \end{aligned} \quad (\text{A. 41})$$

for $r = 1, \dots, 2L$, and similarly, from (8), (A. 28), and (A. 36),

$$\begin{aligned} (B^H \boldsymbol{\gamma}_2(\mathbf{z}))_r &= \frac{2 \sin\left(\frac{\pi M(t - r\Delta t)}{(2M+1)\Delta t}\right) \cos\left(\frac{\pi(M+1)(t - r\Delta t)}{(2M+1)\Delta t}\right)}{\sin\left(\frac{\pi(t - r\Delta t)}{(2M+1)\Delta t}\right)} \end{aligned} \quad (\text{A. 42})$$

for $r = 1, \dots, 2M$.

Substituting (A. 39)–(A. 42) into (A. 38) we obtain

$$\Phi_q(\omega, z) = \left[\begin{aligned} & 1 - \frac{2L}{2L+1} - \frac{2M}{2M+1} + \frac{1}{2L+1} \\ & \times \frac{2 \sin\left(\frac{\pi Lx}{(2L+1)\Delta x}\right) \cos\left(\frac{\pi(L+1)x}{(2L+1)\Delta x}\right)}{\sin\left(\frac{\pi x}{(2L+1)\Delta x}\right)} \\ & + \frac{1}{2M+1} \frac{2 \sin\left(\frac{\pi M T}{(2M+1)\Delta t}\right) \cos\left(\frac{\pi(M+1)t}{(2M+1)\Delta t}\right)}{\sin\left(\frac{\pi t}{(2M+1)\Delta t}\right)}, \\ & \text{for } q = 1, \\ & \frac{1}{2L+1} e^{-j(q-1)\Delta x \omega_x} \\ & \times \left(1 + \frac{2 \sin\left(\frac{\pi L(x - (q-1)\Delta x)}{(2L+1)\Delta x}\right)}{\sin\left(\frac{\pi(x - (q-1)\Delta x)}{(2L+1)\Delta x}\right)} \right. \\ & \quad \left. \times \cos\left(\frac{\pi(L+1)(x - (q-1)\Delta x)}{(2L+1)\Delta x}\right) \right), \\ & \text{for } q = 2, \dots, 2L+1, \\ & \frac{1}{2M+1} e^{-j(q-2L-1)\Delta t \omega_t} \\ & \times \left(1 + \frac{2 \sin\left(\frac{\pi M(t - (q-2L-1)\Delta t)}{(2M+1)\Delta t}\right)}{\sin\left(\frac{\pi(t - (q-2L-1)\Delta t)}{(2M+1)\Delta t}\right)} \right. \\ & \quad \left. \times \cos\left(\frac{\pi(M+1)(t - (q-2L-1)\Delta t)}{(2M+1)\Delta t}\right) \right), \\ & \text{for } q = 2(L+1), \dots, 2(L+M)+1. \end{aligned} \right] \quad (\text{A. 43})$$

Substituting (2), (6), and (A. 43) into (A. 19) and, after some further algebra, we obtain (10). This completes the proof.

REFERENCES

- [1] A. Feuer and N. Maor, "Acquisition of image sequences with enhanced resolution," U.S.A Patent (pending), 2005.
- [2] E. Shechtman, Y. Caspi, and M. Irani, "Increasing space-time resolution in video," in *Proceedings of the 7th European Conference on Computer Vision (ECCV '02)*, vol. 1, pp. 753–768, Copenhagen, Denmark, May 2002.
- [3] K. F. Cheung, "A multi-dimensional extension of Papoulis' generalized sampling expansion with application in minimum density sampling," in *Advanced Topics in Shannon Sampling and Interpolation Theory*, R. J. Marks II, Ed., pp. 86–119, Springer, New York, NY, USA, 1993.
- [4] H. Stark and Y. Yang, *Vector Space Projections*, John Wiley & Sons, New York, NY, USA, 1998.
- [5] N. Maor, "Compression at the source," M.S. thesis, Department of Electrical Engineering, Technion, Haifa, Israel, 2006.
- [6] E. Dubois, "The sampling and reconstruction of time-varying imagery with application in video systems," *Proceedings of the IEEE*, vol. 73, no. 4, pp. 502–522, 1985.
- [7] A. Feuer and G. C. Goodwin, "Reconstruction of multidimensional bandlimited signals from nonuniform and generalized samples," *IEEE Transactions on Signal Processing*, vol. 53, no. 11, pp. 4273–4282, 2005.
- [8] A. Papoulis, "Generalized sampling expansion," *IEEE Transactions on Circuits and Systems*, vol. 24, no. 11, pp. 652–654, 1977.
- [9] A. Feuer, "On the necessity of Papoulis' result for multi-dimensional GSE," *IEEE Signal Processing Letters*, vol. 11, no. 4, pp. 420–422, 2004.

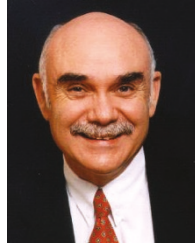
Nir Maor received his B.S. degree from the Technion-Israel Institute of Technology, in 1998, in electrical engineering. He is at the final stages of studies toward the M.S. degree in electrical engineering in the Department of Electrical Engineering, Technion-Israel Institute of Technology. Since 1998 he has been with the Zoran Microelectronics Cooperation, Haifa, Israel, where he has been working on the IC design for digital cameras. He has ten years of experience in SoC architecture and design, and in a wide range of other digital camera aspects. He designed, developed, and implemented the infrastructure of the digital camera products. In particular, his specialty includes the aspects of image acquisition and digital processing together with a wide range of logic design aspects. While being with Zoran, he established a worldwide application support team. He took a major part in the definition of the HW architecture, development, and implementation of the image processing algorithms and other HW accelerators. Later on, he leads the SW group, Verification group, and the VLSI group of the digital camera product line. At the present, he is managing a digital camera project.



Arie Feuer has been with the Electrical Engineering Department at the Technion-Israel Institute of Technology since 1983 where he is currently a Professor and Head of the Control and Robotics Lab. He received his B.S. and M.S. degrees from the Technion in 1967 and 1973, respectively, and his Ph.D. degree from Yale University in 1978. From 1967 to 1970 he was in industry working in automation design and between 1978 and 1983 with Bell Labs in Holmdel. Between the years 1994 and 2002 he served as the President of the Israel Association of Automatic Control and was a member of the IFAC Council during the years 2002–2005. Arie Feuer is a Fellow of the IEEE. In the last 17 years he has been regularly visiting the Electrical Engineering and Computer Science Department at the University of Newcastle. His current research interests include: (1) resolution enhancement of digital images and videos, (2) sampling and combined representations of signals and images, and (3) adaptive systems in signal processing and control.



Graham C. Goodwin obtained his B.S. (physics), B.E (electrical engineering), and Ph.D. degrees from the University of New South Wales. He is currently Professor of Electrical Engineering at the University of Newcastle, Australia and holds honorary Doctorates from Lund Institute of Technology, Sweden and the Technion Israel. He is the coauthor of eight books, four edited volumes, and many technical papers. Graham



is the recipient of Control Systems Society 1999 Hendrik Bode Lecture Prize, a Best Paper award by IEEE Transaction on Automatic Control, a Best Paper award by Asian Journal of Control, and two Best Engineering Text Book awards from the International Federation of Automatic Control. He is a Fellow of IEEE; an honorary Fellow of Institute of Engineers, Australia; a Fellow of the Australian Academy of Science; a Fellow of the Australian Academy of Technology, Science, and Engineering; a Member of the International Statistical Institute; a Fellow of the Royal Society, London, and a foreign Member of the Royal Swedish Academy of Sciences.